Impact of elastomer composition on rubber-toughened organic solar cell performance

Abdullah Al Shafe[1,5], Doan Vu[2,4,5], Subhrangsu Mukherjee[2,5], Jordan Shanahan[3,5], Priyanka Ketkar[6], Wei You[3,5], Dean DeLongchamp[6], Harald Ade[2,5], Brendan O'Connor[4,5]

[1]Department of Materials Science and Engineering, North Carolina State University, Raleigh, NC 27695, USA

[2]Department of Physics, North Carolina State University, Raleigh, NC 27695, USA

[3]Department of Chemistry, University of North Carolina, Chapel Hill, NC, 27514, USA

[4]Department of Mechanical and Aerospace Engineering, North Carolina State University, Raleigh, NC 27695, USA

[5]Organic and Carbon Electronic Laboratories (ORaCEL), North Carolina State University, Raleigh, NC 27695, USA

[6]Material Measurement Laboratory, National Institute of Standards and Technology, Gaithersburg, MD 20899

*Corresponding author: btoconno@ncsu.edu

KEYWORDS. Organic solar cells, Thermoplastic elastomers, Fracture toughness, Miscibility, Mechanical resilience, Polymer blends.

Abstract

Adding a thermoplastic elastomer to an organic solar cell (OSC) active layer has been shown to improve its mechanical resilience while largely maintaining optoelectronic performance. However, a guide to select from the many elastomers available is needed for systematic optimization. Here, we delineate how the structure and composition of the elastomer impact the active layer morphology, fracture toughness, and OSC performance when applied in a high efficiency polymer:small-molecule acceptor active layer. We compare styrene-ethylene-butylene-styrene (SEBS) and styrene-ethylene-propylene-styrene (SEPS) elastomers with varying molecular weight (M_w) and styrene content. The morphology was probed in detail with resonant soft X-ray scattering (RSoXS) and grazing incidence X-ray scattering (GIWAXS). We reveal that the compliant elastomer is more impactful than M_w in improving the fracture toughness. The compliance increases when the styrene content is reduced and when the EP block is employed instead of the EB block. In addition, the improved miscibility of the low-styrene-content SEPS leads to the least disruption of the molecular packing, resulting in maintaining power conversion efficiency the best. These factors lead to the emergence of a Pareto front along the fracture toughness and OSC efficiency dimensions. The optimal combination of mechanical resilience and OSC efficiency was found when incorporating a mass fraction of 7.5 % low-styrene-content SEPS in a PM6:BTP-eC9 active layer. Such OSCs maintained nearly 95% of the neat binary active layer power conversion efficiency while more than tripling the fracture energy. Based on these results, guidelines for elastomer selection and loading are provided to advance rubber-toughened OSCs.

1. Introduction

Target applications of organic solar cells (OSCs) include those that take advantage of their high energy density (W/kg), thin form factor, and flexibility.[1–4] This includes OSCs integrated onto textiles such as clothes and tents, stowable solar modules that can be transported and deployed easily, and indoor energy scavenging for household and office electronics.[5–7] For successful implementation in these applications, it is important that the OSCs are mechanically robust and can withstand a variety of stressors, including object impact and bending without degrading efficiency. This has led to research efforts to not only improve OSC power conversion efficiency, but also mechanical resilience.[8,9] In OSCs, the photo-active layer can be a location prone to mechanical failure.[10–12] Thus, there have been significant research efforts to improve the mechanical performance of the active layer while maintaining high power conversion efficiency (PCE). One approach has been to manage the bulk heterojunction (BHJ) morphology to improve mechanical properties.[13–16] However, this is difficult to accomplish without negatively impacting PCE. Alternatively, efforts have included modifying the organic semiconductor materials to imbue target mechanical properties. This approach has included the development of copolymers with flexible linkers, replacing brittle small molecule acceptors with polymers, and introducing methods to crosslink the photoactive semiconductors.[17–19] These approaches can be effective, yet they often require complex synthesis and processing techniques, which may limit commercial viability.[20,21] Alternatively, a popular and promising strategy is to incorporate insulating polymer additives into the photoactive layer.[22–24] This can significantly improve mechanical resilience while still employing high efficiency polymer:small molecule acceptor (SMA) systems. A common target additive is thermoplastic elastomers, which are known for their stretchability and toughness.[25–28] In our previous work, we demonstrated that styrene-ethylene-butylene-styrene (SEBS) can enhance the fracture toughness of the active layer while largely maintaining OSC efficiency.[29] The

SEBS was found to be miscible with the donor/acceptor layer at a mass fraction of approximately 5 %. Adding slightly more SEBS than the miscible limit was found to significantly increase the cohesive fracture energy (G_c) of the active layer relative to the neat blend, with only a minor decrease in PCE. This improvement in G_c represented a record in the G_c·PCE (7 J/m^2 and 11.9 %) figure of merit and was attributed to the SEBS's ability to redistribute the strain energy near the crack tip. Similarly, Zheng et al. used a styrene-ethylene-propylene-styrene (SEPS) thermoplastic elastomer to make stretchable OSC devices.[30] They found an enhanced balance of stretchability and efficiency with a mass fraction of 5-10 % (5-10 wt%) elastomer loading. Their results also showed no aggregation of the SEPS with the addition of up to a mass fraction of 5 % and only a minor decrease in PCE.

When considering the SEBS and SEPS elastomers, SEBS is generally a harder elastomer with greater toughness than SEPS, which is attributed to the more crystalline ethylene-butylene (EB) group. In both cases, the polystyrene (PS) content, which forms hard physical crosslinks, influences a number of properties of the elastomer, including stiffness and toughness.[31,32] The weight-average molecular weight (M_w) of the elastomer is another important consideration that can influence processing and mechanical properties.[33,34] For example, the Bao group mixed a series of SEBS with varying M_w with a polymer semiconductor and observed increased segregation of the elastomer in the polymer matrix with higher M_w.[35] They attributed this behavior to the reduced entropic gain in the free energy of mixing for higher molecular weight polymers, which reduces miscibility. Thus, the various attributes of the elastomer, including the soft block structure, the PS content, and M_w, are key factors that may have a significant impact on rubber-toughened OSC performance.

In this work, we determine the impact of two different elastomers, SEBS and SEPS, with varying M_w and styrene content on OSC optoelectronic and mechanical performance. We add the elastomers to a PM6:BTP-eC9 bulk heterojunction (BHJ) OSC. This is a widely studied polymer:SMA BHJ that represents a model system.[36,37] The molecular structure of the semiconductors and elastomers utilized is given in **Figure 1**. We first report the miscibility of the elastomers in the photoactive layer. This is investigated using a combination of surface energy measurements and resonant soft X-ray scattering (RSoXS). The length scale of the segregated elastomer domains was also estimated from the RSoXS. We utilized grazing incidence wide angle X-ray scattering (GIWAXS) to understand how various elastomers impact the molecular packing of the semiconductors. The cohesive fracture energy of the photoactive layer is then reported, which was evaluated using four-point bend (FPB) tests. Finally, the OSC device performance is summarized. Through this comprehensive analysis, a Pareto front emerges for elastomer addition optimization from which we establish key morphological drivers that improve fracture toughness while minimizing the negative impact on OSC PCE. In particular, we find that low-compliance elastomers maximize fracture toughness. In addition, the elastomers that have greater miscibility minimize the penalty in OSC efficiency. In the systems analyzed, we found that low-styrene-content SEPS can be added to the active layer at up to a mass fraction of 7.5 % while maintaining more than 95% of the PCE of the control OSC, and more than triples the active layer fracture energy. Based on the results of this work, we provide clear guidelines for elastomer selection and loading to optimize rubber-toughened OSC performance.

2. Results and Discussion

2.1. Elastomer properties

Six different elastomers were selected for study: three SEBS and three SEPS. The elastomers consist of PS end blocks with a central block made of ethylene-propylene (EP) in SEPS and EB in SEBS. The three elastomers considered for each type had differences in M_w and PS fraction. The molecular weight and the amount of PS content of each elastomer are given in **Table 1**. We designate each elastomer based on the mass fraction of PS content, elastomer type (P for SEPS or B for SEBS), and then the number average molecular weight, M_n (e.g., $18P_{130}$). The thermal transition behavior of the elastomers was measured using dynamic mechanical analysis (DMA), with the storage modulus, loss modulus, and the tan (δ) profiles given in the supplementary information (SI) **Figure S1(a-f)**. The inner block and styrene blocks show distinct glass transition temperatures, which we label as T_β and T_α.[38] The lower temperature transitions are associated with the EP or EB blocks,[39–41] and the higher temperature transitions are associated with the styrene blocks.[42] The transitions are characterized by the peak of the loss modulus curves. We find that T_β ranged from -51.5 °C to -49.5 °C, while the T_α ranged from approximately 60 °C to 110 °C. These transition temperatures, presented in **Figure S2** and in **Table S1**, both correlate with the molecular weight of the elastomers, consistent with the Flory-Fox equation.[43] We selected elastomers across a matrix of compositions including PS content, M_w, and soft block structure. While the PS content and M_w both vary across the elastomers considered, the selected elastomers have distinct behavior, enabling us to isolate the impact of these parameters on mechanical and optoelectronic performance.

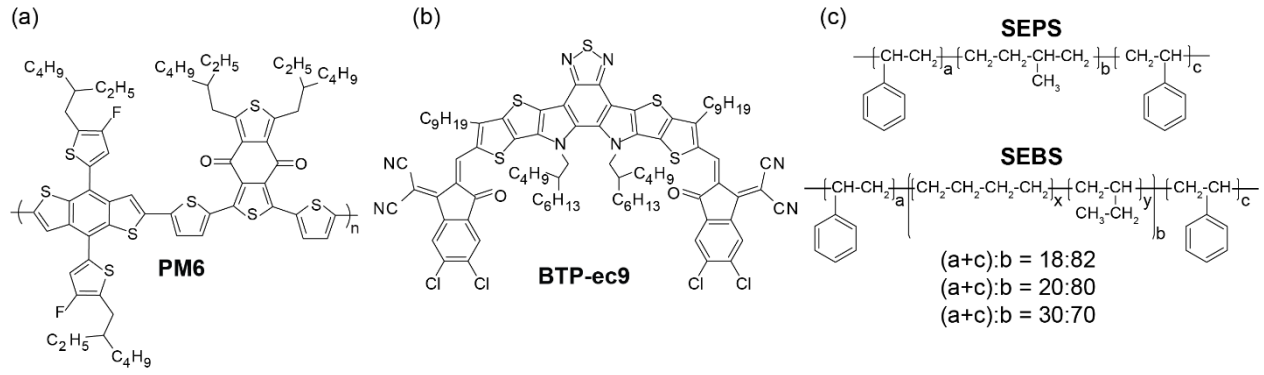

Figure 1. (a-b) Molecular structure of polymer donor PM6 and small molecule acceptor BTP-ec9. (c) Molecular structure of SEPS and SEBS elastomers, along with the constitution of the elastomers considered.

Table 1. Elastomer designation, their polystyrene content, number- and mass-averaged molecular weights.

Elastomer type	Elastomer designation	PS content (mass fraction %)	M_n (kg/mol)	M_w (kg/mol)
SEPS	$18P_{130}$	18	125.7	136.9
	$20P_{300}$	20	300.6	345.0
	$30P_{70}$	30	71.8	77.3
SEBS	$18B_{140}$	18	143.8	186.8
	$20B_{110}$	20	112.7	135.6
	$30B_{180}$	30	175.7	216.8

2.2. Active layer morphology and miscibility with elastomer addition

The differences in miscibility of the elastomers with the organic semiconductors were first investigated through surface energy analysis. The surface energy can be used to estimate the Flory-Huggins interaction parameters (χ), which provide insights into the miscibility of the elastomers with the PM6:BTP-eC9 blend. The χ values were estimated using $\chi \propto (\sqrt{\gamma_A} - \sqrt{\gamma_B})^2$, where γ_A

and γ_B are surface energies of component A and B.[44] A closer match in surface energy between the elastomer and the semiconductors results in a lower χ, indicating more favorable interactions and greater miscibility.[45] The surface energy of a neat PM6, neat BTP-ec9, PM6:BTP-eC9 blend, and the elastomers are given in **Figure 2(a)**. The surface energy is calculated based on deionized (DI) water and dimethyl sulfoxide (DMSO) contact angles, which are summarized in the experimental section. The neat PM6 and BTP-ec9 show surface energy values of approximately 29 mN/m and 35.2 mN/m, respectively. The elastomers show a wider variation in surface energy ranging from approximately 29.7 mN/m to 34 mN/m (**Figure 2(a)**). In general, the surface energy of elastomers is driven by both the styrene content and M_w. Elastomers with a higher PS fraction exhibit higher surface energy,[46,47] and lower M_w elastomers with a higher density of chain ends can influence the surface energy depending on the nature of the end groups.[48,49] In the present case, the elastomer surface energy was most strongly correlated with PS content for both SEPS and SEBS. Based on the surface energy, χ of the various materials with PM6 and BTP-ec9 are given in **Figure 2(b, c)**, and **Table S2**. This trend results in χ for PM6 and elastomers having a positive correlation with elastomer styrene content (**Figure 2(b)**). We find the opposite trend when considering χ between BTP-ec9 and the elastomer (**Figure 2(c)**) where the higher styrene content results in a lower χ.

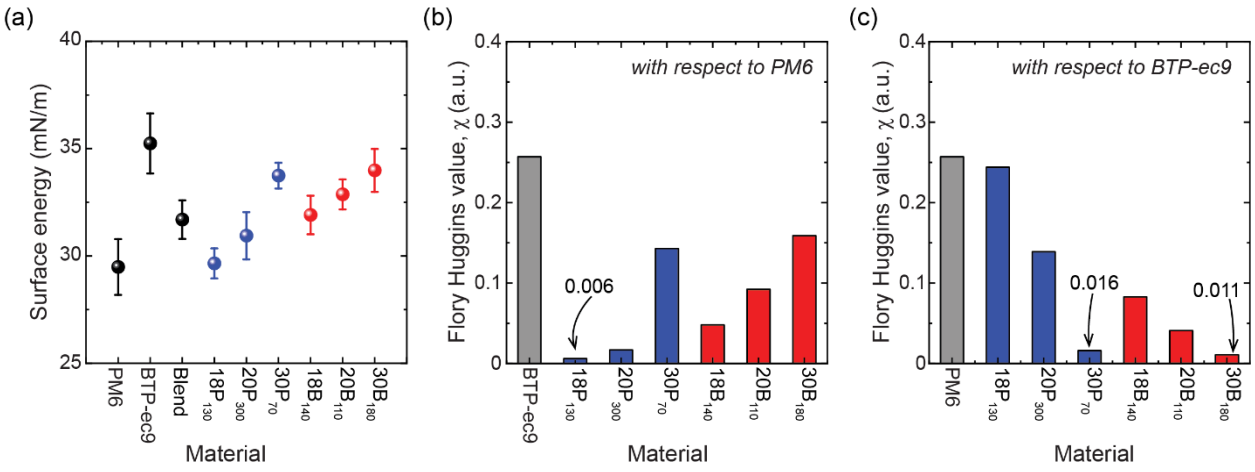

Figure 2. (a) Surface energy of organic semiconductors and elastomers studied, measured from contact angle analysis. Error bars represent one standard deviation from the mean of replicate measurements. (b) Flory-Huggins' interaction parameter, χ with respect to polymer donor PM6. (c) χ parameter with respect to small molecule acceptor BTP-ec9. In all figures, black/grey represents neat semiconductors or blend, blue represents the SEPS added blends, and red represents the SEBS added blends.

The phase segregation of the photoactive layer with elastomer addition was probed through RSoXS analysis. The thickness-normalized, Lorentz-corrected, RSoXS intensity profiles for $18P_{130}$ and $18B_{140}$ added PM6:BTP-eC9 blends at various loadings are shown in **Figure 3(a,b)**. The scattering profiles are plotted at an X-ray energy of 284.5 eV. Energy-dependent RSoXS measurements (**SI Figure S3**) confirm that ~284.5 eV provides the strongest contrast between the PM6:BTP-eC9 donor-acceptor phase as well as semiconductor: elastomer domains, consistent with our previous report.[29] The RSoXS data for the other elastomer blend films are given in **Figure S4**. The neat PM6:BTP-eC9 blend exhibits a scattering peak at 0.087 nm^{-1}, corresponding to a domain spacing of 72 nm. This peak is attributed to the nanoscale variations in the scattering length density resulting from the segregation of polymer donor rich and nearly pure SMA domains.[50,51]

With the addition of 5 % mass fraction of $18P_{130}$, the peak position remains close to that of the neat blend, indicating no distinct elastomer segregation. However, as the $18P_{130}$ loading increases to a mass fraction of 10 %, a distinct second peak emerges at a higher q value (0.27 nm^{-1}), with a corresponding domain spacing of 23.2 nm (**Figure S5(a)**). This second peak indicates the formation of a segregated elastomer phase.[29] As peak 2 appears at a q-value approximately three times that of peak 1, it is not a higher-order reflection (e.g., third-order Bragg peak) of the same domain spacing. **Figure S6** confirms this by showing that the extracted domain spacings are not harmonically related, indicating distinct scattering origins for the two peaks. Interestingly, at 7.5 % mass fraction $18P_{130}$ loading, a peak at 0. 11 nm^{-1} is observed, lying between the peak intensities of the 5 % and 10 % mass fraction loadings. Given prior determination of the miscibility with RSoXS in a related system,[29] this is likely due to the miscibility limit being close to the mass fraction of 7.5 %, beyond which a distinct segregated phase is observed. In contrast, adding $18B_{140}$ to the BHJ film at a mass fraction of 5 % results in the emergence of a subtle small spacing domain peak (**Figure S5(b)**) which becomes more distinct at a mass fraction of 7.5 % loading. This indicates that $18B_{140}$ has lower miscibility compared to the similar SEPS formulation ($18P_{130}$).

To compare the miscibility threshold across all elastomers, the elastomer loading at which the second (small domain) peak appears is shown in **Figure 3(d)**. In general, SEPS was found to have slightly greater miscibility with the semiconductors compared to SEBS, with $18P_{130}$ being distinctly more miscible. This is consistent with the surface energy analysis where SEPS had a smaller χ-parameter than the SEBS counterpart with respect to PM6, with $18P_{130}$ having the lowest χ. The segregated domain spacings obtained from peak 1 and peak 2 for the elastomer added blends are summarized in **Figure 3(c)**, **Figure S6**, and in **Table S3**. In all the blends investigated, the domain spacings corresponding to peak 2, which appear with elastomer addition are of similar size

varying between 23 - 33 nm. We have also provided RSoXS profiles of intensity vs q (without Lorentz correction) for all elastomer-added blends in **Figure S7**. It is evident from the figure that the peak locations for the secondary peaks related to segregated elastomer domains are similar in the intensity vs q as the Lorentz corrected RSoXS profiles. Once the elastomer exceeds its miscibility limit, it segregates into kinetically trapped pure domains whose spacing is governed by interfacial tension, diffusion, and solvent evaporation. These factors are similar across the elastomers studied, leading to similar domain spacing. The intrinsic OSC domain spacing captured by RSoXS is attributed to the segregation of a polymer semiconductor rich phase and SMA phase.[29,52] It varies more than the domain spacings corresponding to peak 2, arising from the elastomer. These large donor:acceptor domains do not show a clear trend with styrene content or M_w. Yet there is a positive correlation of the domain spacing with elastomer loading. The SEBS addition also leads to larger domain sizes as compared to the SEPS addition, as shown in **Figure 3(c)**. The segregation in the blend during film solidification has a thermodynamic and kinetic component. Since the addition of the elastomer generally increases the viscosity of the ink, the morphology formation and film drying kinetics will be impacted. Higher viscosity requires an increase in the spin cast speed compared to the neat BHJ to achieve similar film thickness. To maintain a similar film thickness across samples, the spin casting speed was varied as summarized in the experimental section (**Table S4**). This variation in casting conditions and related drying dynamics may contribute to the differences in the observed segregated domain spacing. We found that SEBS addition results in more viscous inks relative to SEPS addition. Viscosity measurements of neat elastomers diluted in chloroform indicate that SEBS exhibits higher viscosity than SEPS, as shown in **Figure S8**. Thus, the viscosity of the resultant blends may be a contributing factor in the observed differences in the spacing of the large domains.

To probe the details of molecular packing and morphology of the BHJ films, we have performed GIWAXS measurements on the various active layer films. The neat PM6:BTP-eC9 blend film exhibits preferential face-on packing with clear (100) lamellar scattering in-plane (IP) and (010) π-π stacking scattering predominantly out-of-plane (OOP), as shown in **Figure S9(a)**. The face-on structure is beneficial for vertical charge transport in OSCs.[12,53] With 5 % mass fraction elastomer addition, the BHJ still maintains a preferential face-on packing structure as evidenced by the out of plane (010) π-π GIWAXS peak (q = 1.72 Å^{-1}), as shown in **Figure S9(b,c)** and **Figure S10**. Increasing the elastomer loading to the mass fraction of 10 % resulted in stronger scattering from the elastomer as characterized by an amorphous halo at q = 1.32 Å^{-1} (**Figure S11**). This broad amorphous scattering is clearly seen in the OOP line cuts given in **Figure S9(d,e)** and **Figure S11**. The addition of the elastomers was found to have a significant influence on the IP (100) lamellar spacing as shown in **Figure 3(e)**. With increased elastomer loading there is a fluctuation in d_{100} spacing. Between the elastomer types, the SEBS is found to increase the d_{100} spacing more than the SEPS counterpart. In fact, the d_{100} spacing is found to decrease slightly with the 5 % mass fraction addition of $18P_{130}$ and $20P_{300}$. In addition, for 10 % mass fraction loading, the elastomers with greater styrene content show more intense scattering of the amorphous halo relative to the out of plane π-π scattering peak of the semiconductors, as summarized in **Figure 3(f)**. This is attributed to the styrene blocks having a stronger scattering cross section than the other elastomer blocks and potential disruption of the organic semiconductor packing order. The disruption of semiconductor packing order with elastomer addition is consistent with the observed increase in d_{100} spacing with elastomer loading. These variations in lamellar spacing reflect changes in local packing interactions between PM6 and BTP-eC9 when elastomers are introduced. Because elastomers modify molecular interactions and film-formation kinetics, fluctuation in d_{100}

spacing suggests the disrupted packing with elastomers addition. The crystal coherence length (CCL) of (100) is shown in **Figure S12**, with the addition of elastomers resulting in a decrease in CCL in the lamellar direction, affirming the disruption of the packing.

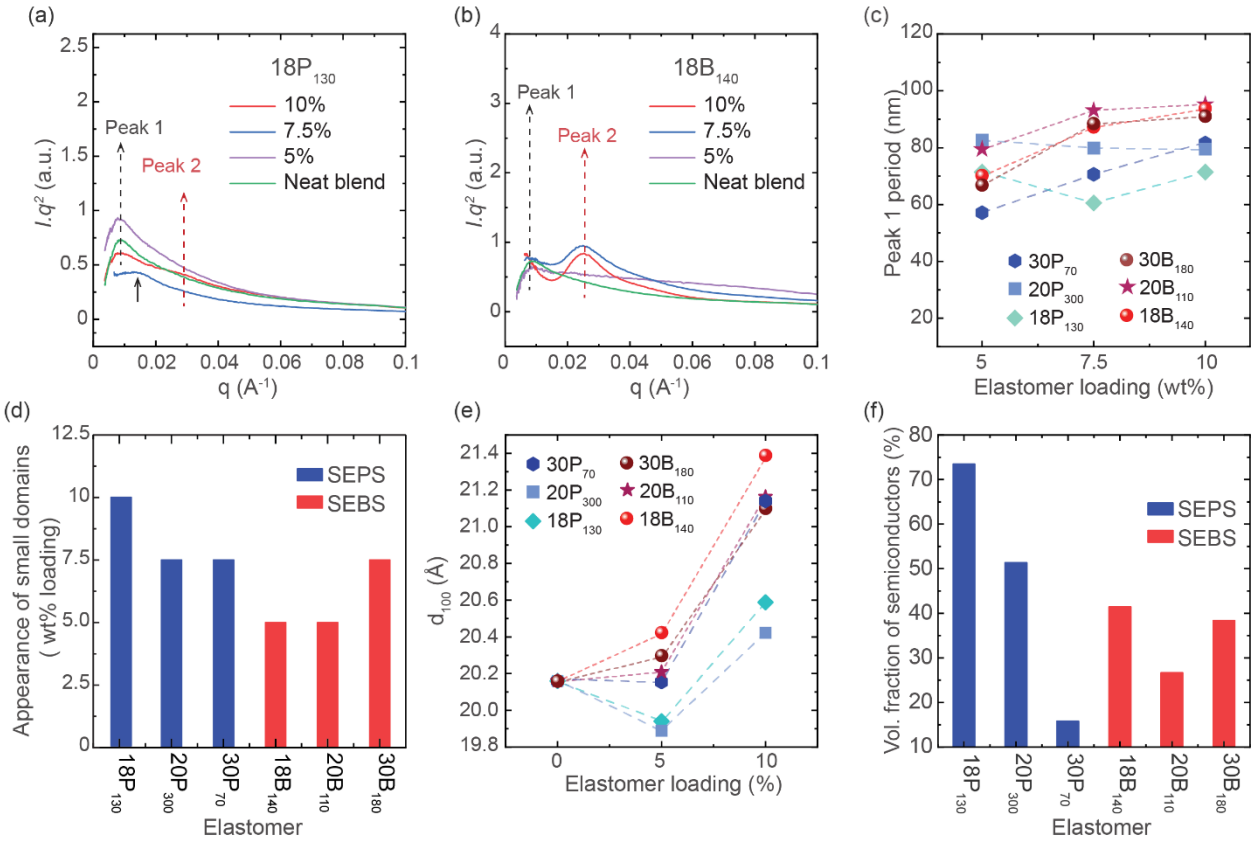

Figure 3. Lorentz-corrected and thickness-normalized RSoXS profiles of thermally annealed PM6:BTP-eC9 blends acquired at 284.5 eV for (a) $18P_{130}$ and (b) $18B_{140}$. (c) Summary of Peak 1 spacing with elastomer loading. (d) The elastomer loading where the peak 2 domain is first observed in the RSoXS data. (e) Lamellar spacing (d_{100}) extracted from GIWAXS measurements as a function of elastomer loading in the SEPS and SEBS elastomer-modified blends. (f) The ratio of the organic semiconductor π-π scattering to the elastomer amorphous halo scattering for the SEPS and SEBS added blends at a mass fraction of 10 % loading. The magnitude of each scattering

feature is determined from the fitted peak areas along the OOP direction in the GIWAXS measurements.

2.3. Fracture Energy

The mechanical resilience of the active layer is characterized through the cohesive fracture energy (G_c) measured using the FPB technique as detailed previously.[54] A higher G_c helps ensure that the material can withstand mechanical stresses without crack propagation, indicating improved mechanical durability.[10,11] The FPB sample structure used to measure the G_c is shown in **Figure 4(a)**. The G_c values for various elastomers at the mass fractions of 5 % and 10 % loading are given in **Figures 4(b**) and **4(c)**, respectively. All load displacement curves from the FPB measurements are given in **Figure S13**. The neat PM6:BTP-eC9 blend shows a G_c value of 2.9 J/m^2, which is similar to other reported polymer:SMA systems.[29,55] The addition of the elastomer improved the fracture energy of the active layer in all cases. At a given elastomer loading, the SEPS-based blends generally exhibit higher G_c values compared to their SEBS counterparts. The favorable G_c values in SEPS are particularly evident at a mass fraction of 5 % loading as given in **Figure 4(b)**. In this case, the $18P_{130}$ elastomer-based films achieved a G_c of close to 8 J/m^2, while the $18B_{140}$ elastomer-based films were approximately 6 J/m^2. At the mass fraction of 10 % loading, the gap narrows slightly but SEPS still maintains a higher G_c. We have also measured the G_c value of the mass fraction of 7.5 % $18P_{130}$ and $18B_{140}$ added blends, which are 10 J/m^2 and 8 J/m^2, respectively (**Figure S14**). We attribute the greater G_c in SEPS over SEBS to the amorphous nature EP segment over the modest crystallinity of EB segments increasing the elastomer compliance, discussed further below.

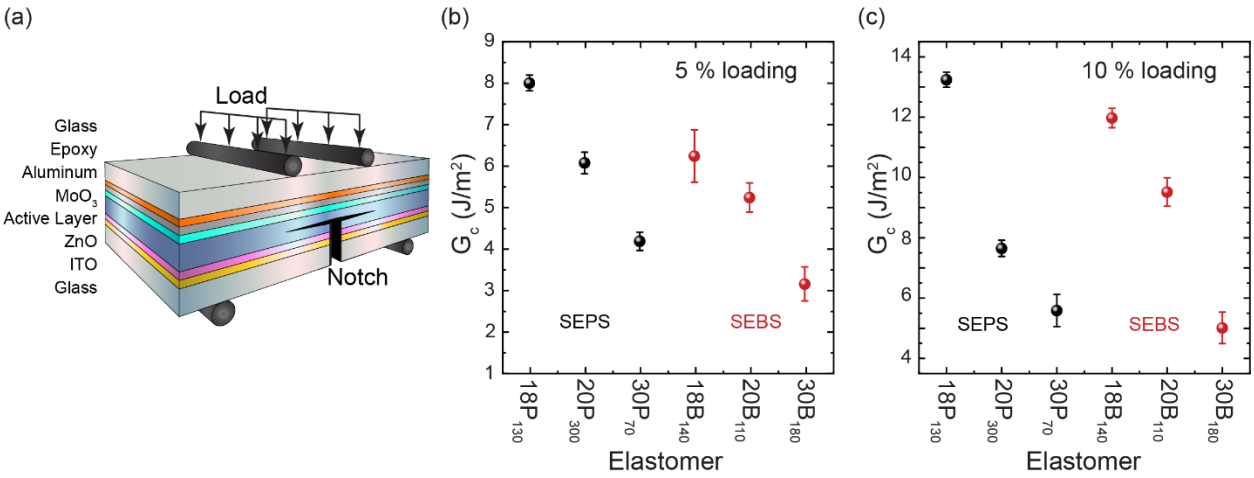

Figure 4. (a) Schematic of the four-point bend structure used for measuring cohesive fracture energy, G_c. (b) G_c of the mass fraction of 5 % elastomer added PM6:BTP-eC9 blends for both SEPS and SEBS series. (c) G_c of the PM6:BTP-eC9 blends for the mass fraction of 10 % elastomer loading. Error bars represent one standard deviation from the mean from multiple measurements.

2.4. Photovoltaic characteristics

The OSC device structure fabricated in this work is provided in **Figure 5(a)**. The PCE of the cells with varying SEPS and SEBS loading is given in **Figures 5(b, c)**. It is evident that increasing the elastomer content generally leads to a decline in PCE. Yet, the extent of the PCE decline depends on the elastomer used. The OSCs that employ $18P_{130}$ exhibit a gradual reduction in PCE with increased loading, retaining over 95% of its initial PCE with the mass fraction of 7.5 % loading. The SEBS-based devices experienced a slightly sharper decline with loading, with $18B_{140}$ falling below the 95% PCE threshold at the same mass fraction of 7.5 % loading. Lastly, it was found that the addition of the high styrene content SEPS, $30P_{70}$, showed the strongest decline in PCE at low elastomer loading. In addition to PCE, other photovoltaic parameters, including short-circuit current density (J_{sc}), fill factor (FF), and open-circuit voltage (V_{oc}), exhibit distinct trends as shown in **Figures 5(e)**, **Figure 5(f)**, and **Figure S15**. The details of the photovoltaic parameters

are summarized in **Table S5**. For $18P_{130}$-based devices, J_{sc} shows an increase at the mass fraction of 5 % elastomer loading, similar to what we observed in our previous report of elastomer toughened OSCs, suggesting reduced recombination losses.[29] The other SEPS and SEBS based devices display a more consistent reduction in J_{sc} across all concentration. Interestingly, the addition of 5 wt% elastomer results in a drop in V_{oc} that than increases slightly with increased elastomer loading. While the change in V_{oc} with loading is small, it does appear to be a statistically significant change for both SEPS and SEBS based devices. This aligns with previous studies where it has been found that elastomers or insulating polymer (e.g., polystyrene) additions can leading to a slight V_{oc} enhancement, attributed to reduced non-radiative recombination.[56] Here, we believe the initial V_{oc} drop is associated with disruption of the polymer semiconductor packing order. With increasing elastomer loading, the dielectric environment of the photoactive layer decreases resulting in a shift in charge transfer energy that resulted in an increase in V_{oc}. However, further research is needed to fully understand this behavior. The fill factor dropped slightly with the inclusion of the elastomers but still maintained values of over ~65 % with a mass fraction of 7.5 % loading or less, and was relatively constant over all elastomer loadings. Absolute dark J-V curves for $18P_{130}$ are presented in **Figure S16**. At different elastomer loadings, composition-dependent changes in forward current with increased resistive-like losses are evident. The progressive increase in series resistance with higher elastomer loading directly contributes to losses in J_{sc} and FF observed in device performance.

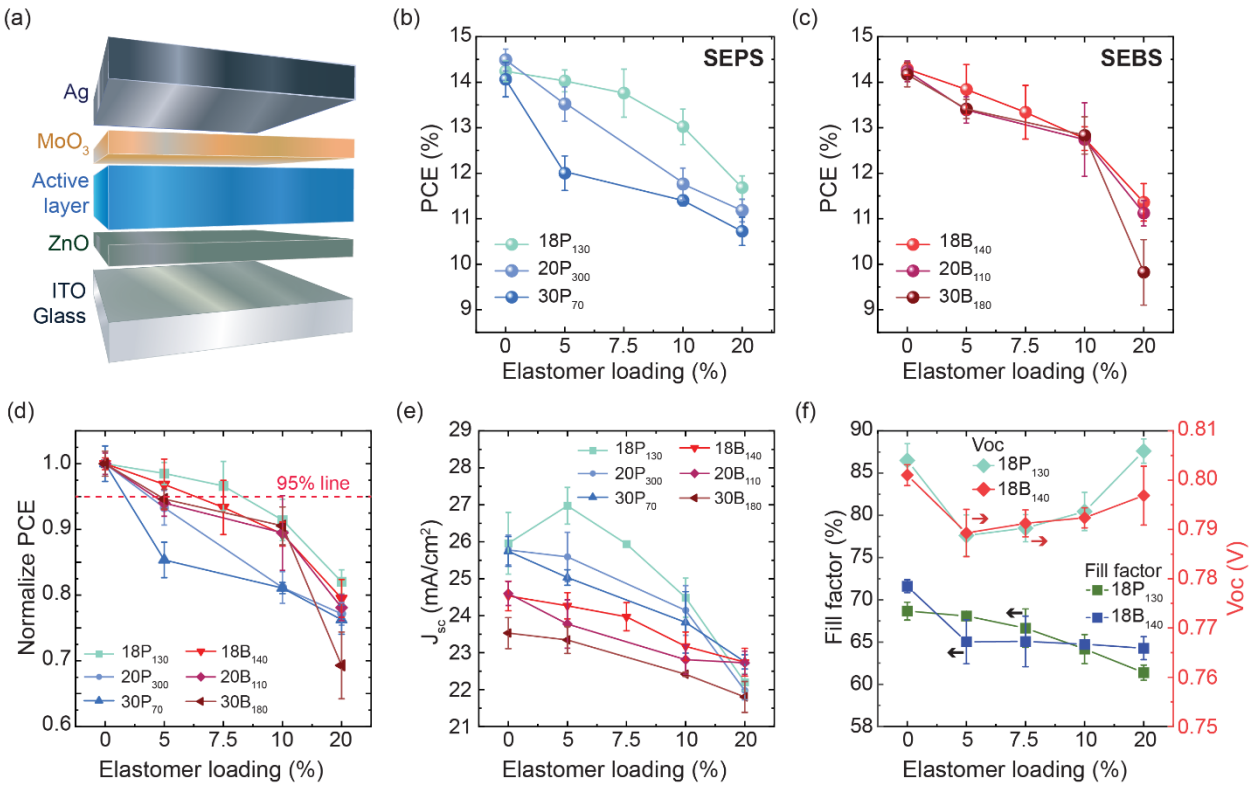

Figure 5. (a) Structure of the organic solar cell device used in this study. (b-c) PCE of different SEPS and SEBS added devices at different loadings. (d) Normalized PCE for all devices. (e) J_{sc} values from all SEPS and SEBS added devices. (f) V_{oc} and FF values for $18P_{130}$ and $18B_{140}$ added devices. Error bars represent the one standard deviation from the mean from multiple measurements

2.5. Elastomer characteristics that drive mechanical and optoelectronic performance

For the elastomers examined, we find differences in segregation behavior, fracture toughness, and OSC efficiency. While there is a convolution of M_w, styrene content, and soft-block structure for the elastomers analyzed, several clear correlations can be established that guide future development of rubber-toughened OSCs. In all cases, the elastomer addition supports crack path deflection and partial miscibility of the segregated domains to support load transfer. There is a clear increase in fracture energy with elastomer loading in all cases, which is commonly observed

in rubber toughened OSCs.[29] There is also a gradual efficiency drop off with increased elastomer addition. Due to the efficiency drop off at high elastomer loading, we limited the loading to under 20 % mass fraction and largely focused on the addition of 5-10 % mass fraction.

Over the elastomer loading range of 5-10 % mass fraction, fracture toughness improved when reducing the styrene content of the elastomer, and SEPS was found to be favored over SEBS when comparing similar styrene loading (**Figure 4**). This trend is not fully reflected in the segregation behavior of the elastomers, and there was no clear correlation with the M_w of the elastomer. Given that the PS acts as glassy physical cross-link sites, the M_w between cross-link sites may drive behavior more than the total polymer M_w. Instead, the changing mechanical properties are most strongly associated with elastomer stiffness. Both SEPS and SEBS are tri-block copolymers. However, the EB block in SEBS can crystallize while the ethylene-propylene block in SEPS is amorphous.[57,58] Because of this lack of crystallinity, SEPS is more compliant than SEBS when considering similar styrene content. This aligns with the stress-strain characteristics of the neat elastomers, shown in **Figure S17**. From the stress-strain curves, we find that the SEPS has a lower Young's modulus compared to SEBS for similar styrene content. The inverse of Young's modulus (e.g., compliance) correlates well with the BHJ fracture energy at 5 % mass fraction loading, given in **Figure 6(a)**. We also find a correlation between the fracture toughness and the relative GIWAXS scattering intensity of the elastomer to the semiconductor π-π stacking, as shown in **Figure S18(a)**. The relative scattering intensity from the elastomer will be in part driven by the styrene density. The increase in styrene content also increases the elastomer stiffness, and thus, the elastomer stiffness may be behind this correlation. Yet, the scattering ratio may also be from disruption of π- π stacking order, which may contribute to increasing toughness. However, the high coefficient of determination for the relationship between compliance and fracture toughness

suggests that this is the dominant elastomer characteristic that drives fracture energy. This behavior is attributed to the ability of the more compliant elastomer to take on the strain energy near the crack tip, reducing the local stress concentration that would lead to crack growth.

Turning to the OSC efficiency, many of the systems follow a similar trend with elastomer loading (**Figure 5(a-c)**), showing a gradual reduction in efficiency with increased loading. Yet, there are some differences depending on the elastomer with $18P_{130}$ showing the lowest decline and $30P_{70}$ showing the largest decline in PCE with loading. To understand this behavior, we consider the morphological differences in the active layer. The RSoXS does not show a significant difference in the domain spacing that is associated with the segregation of PM6 and BTP-ec9 when adding the elastomer, and thus this is not a primary driver of the efficiency difference. The GIWAXS measurements reveal that the elastomer addition increases the d_{100} spacing of the semiconductors and that the increase in d-spacing is greater for SEBS addition relative to SEPS, with the exception of $30P_{130}$ (**Figure 3(e)**). Similarly, the scattering ratio of the (010) semiconductor peak to the elastomer decreases with increased styrene content (**Figure 3(f)**), with the largest ratio found for $18P_{130}$ and the lowest ratio found for $30P_{70}$. Herman's orientation parameter (S) based on the distribution of the (010) peak of the semiconducting materials was calculated and shown in **Figure S18(b**). The S parameter ranges from 1 to -0.5, corresponding to a complete face-on to edge-on orientation with azimuthal angle normal to the substrate.[59] The S-parameter ≈ 0.25 of the as-cast film suggests the preferential face-on orientation, and the S-parameter decreases with increasing elastomer loadings, suggesting the decrease in degree of face-on orientation induced by elastomer incorporation. The changing S-parameter is relatively consistent with the drop in J_{sc} and FF across elastomer composition and concentration. Therefore, the disruption of the local packing order and decrease in face-on orientation of the semiconductor

with elastomer addition is likely the primary driver for efficiency drop-off. Prior work has shown that the decrease in face-on orientation negatively impacts the charge transport and photovoltaic performance .[60] The elastomer that causes the least packing disruption ($18P_{130}$) maintains device efficiency the best with increasing loading, whereas the elastomer with the most disruption ($30P_{70}$) shows the steepest PCE decline. Notably, lamellar spacing is lowest for the $18P_{130}$ elastomer compared to other elastomers at 5 % mass fraction loading, which correlates with an increase in J_{sc}. It is difficult to say what drives this packing disruption. The decrease in CCL with the incorporation of elastomers is consistent with the decrease in photovoltaic performance. However, $18P_{130}$ was found to have the greatest miscibility, and thus this is not a key driver for disruption and may in fact enable maintenance of semiconductor ordering.

A comparison of the active layer fracture energy and OSC efficiency is given in **Figure 6(b)**. We see a Pareto front emerge across the systems examined. In optimizing both OSC efficiency and mechanical resilience, we see that $18P_{130}$ is consistently at the frontier. Thus, the low stiffness elastomer marked by low styrene content and the EP block is key to optimizing efficiency and toughness. Taking the results collectively allows for a schematic map of the desired properties in polymer:SMA OSCs that optimize rubber-toughened OSCs, illustrated in **Figure 6(c)**. The driving factors to push the system into the upper right quadrant of the plot (maximizing G_C and PCE) is to employ a high compliance elastomer with high miscibility that minimizes that disruption of the semiconductor packing order. The elastomer loading should be near the miscibility threshold, where further addition results in a more dramatic drop in PCE.

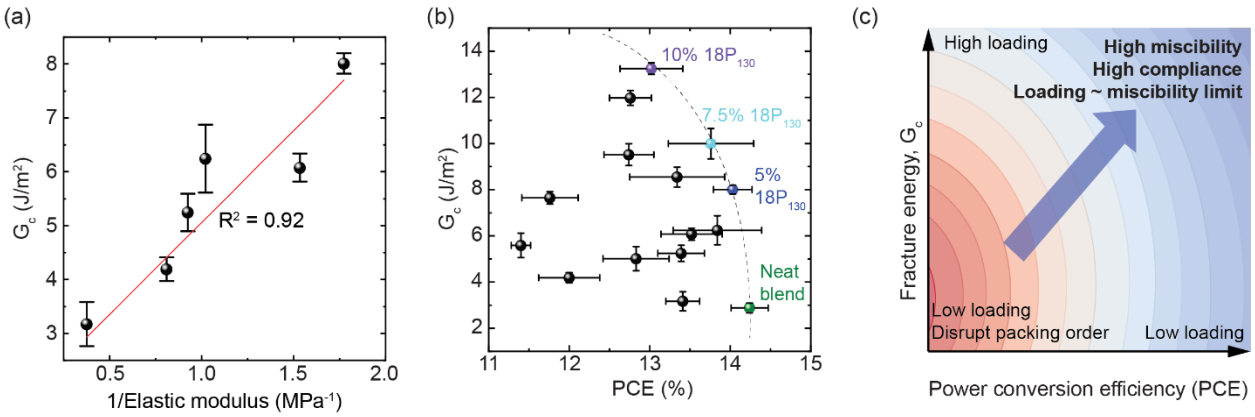

Figure 6. (a) Correlation between cohesive fracture energy (G_c) and the compliance (inverse of the elastic modulus) of the neat elastomers. (b) Pareto analysis of G_c versus PCE for OSCs with the different elastomer compositions. (c) Schematic design map summarizing the elastomer consideration that maximizes G_c and PCE. Error bars represent one standard deviation from the mean from multiple measurements.

3. Conclusion

The elastomer selection and loading in rubber-toughened OSCs has a large impact on fracture toughness and device efficiency. In this work, we investigated the addition of two elastomer types, SEPS and SEBS, with a variation in M_w and styrene content to PM6:BTP-eC9 based OSCs. Our analysis revealed minor differences in miscibility, which varied from approximately 5 to10 % in all cases. There was also no clear correlation between the elastomer M_w and the improved fracture energy observed. Elastomers with greater compliance, e.g., low PS content and an EP block, were found to be the primary factor driving increased fracture energy. A compliant elastomer is likely to more readily take on the strain energy near the crack tip and reduce the stress concentration at the crack tip. While the present work focuses on intrinsic cohesive fracture energy as a primary measure of mechanical robustness, future studies incorporating cyclic bending or stretching tests would provide additional insight into long-term durability under repeated mechanical deformation.

In all elastomers studied, the OSC power conversion efficiency reduces with increased elastomer addition. The increased elastomer loading was not found to change the phase segregation of the semiconductor blend significantly. However, the elastomer addition did impact the local semiconductor packing order as observed by a relative decrease in X-ray scattering intensity of the (010) peak and changes in the (100) d-spacing. The changes in scattering were similar across elastomers, with the exception that the elastomer with the greatest miscibility ($18P_{130}$) had the lowest packing disruption. This suggests that improving elastomer miscibility may be a route to maintain power conversion efficiency while improving the fracture toughness of the active layer. As a result of these factors, $18P_{130}$ was the best performing elastomer evaluated, where a mass fraction of 7.5 % addition into the active layer was found to maintain over 95% of the neat active layer PCE while increasing the fracture energy by a factor of three.

From these results, design guidelines for rubber-toughened OSCs can be made, as summarized in **Figure 6(c)**. First, it is preferred to lower the stiffness of the elastomer, particularly by reducing the rigid block fraction in a tri-block copolymer. Second, an elastomer that minimizes disruption of local semiconductor packing order is favored to maintain OSC efficiency. In this study, it was found that the most miscible elastomer ($18P_{130}$) suggests that improving elastomer miscibility may be a route to reducing efficiency drop-off. While the elastomers examined have similar miscibility with the photoactive layer, slight improvements, particularly with the polymer semiconductor, can have a significant impact on the optimization of fracture toughness and PCE. Lastly, the elastomer loading should be near the miscibility threshold for the optimal balance of fracture toughness and PCE. Significantly increasing the elastomer loading results in a pronounced drop off in PCE limiting the viability of the approach. **4. Experimental Section**

Materials: PM6 (M_w ~ 120 kg/mol, PDI ~ 2.8) and BTP-ec9 were purchased from 1 Material Inc. Styrene-ethylene-propylene-styrene (SEPS) elastomers (SEPTON series) were obtained from Kuraray America, Inc., while styrene-ethylene-butylene-styrene (SEBS) elastomers (TUFTECTM series) were sourced from Asahi Kasei. Zinc acetate, ethanolamine, and 2-Methoxyethanol (anhydrous) were bought from Sigma-Aldrich. The two-part thermosetting epoxy (EPO-TEK 353 ND) was supplied by Epoxy Technology, Inc. Certain commercial equipment, instruments, and materials are identified in this paper to foster

understanding. Such identification does not imply recommendation or endorsement by the National Institute of Standards and Technology, nor does it imply that the materials or equipment identified are necessarily the best available for the purpose.

Device fabrication: Devices were fabricated on indium tin oxide (ITO)-coated glass substrates. Initially, the ITO-coated glass substrates were cleaned by sonication for 15 minutes in deionized water (DI), acetone, and isopropanol, followed by a 15-minute UV-ozone treatment. To prepare the ZnO solution, 110 mg of zinc acetate was dissolved in 1 mL of 2-methoxyethanol solvent, mixed with 30.5 µL of ethanolamine, and stirred overnight at room temperature. This ZnO solution was spin-coated onto the ITO substrates at 6,000 rpm ((1 rpm = 2π per 60 rad s^{-1})) for 50 s, forming a 30–35 nm thick film, which was then annealed at 150 ˚C for 15 min. For the active layer, materials were mixed at a ratio of 1:1.2 with a concentration of 15 mg/mL in chloroform (CF) and stirred for at least 3 hours at 45 ˚C using a magnetic stirrer. The solution was dynamically cast onto the ZnO layer by spin-coating at 2,000–3,600 rpm for 30 s and subsequently annealed at 100 ˚C for 10 minutes. The spin coating speed was varied to achieve a common film thickness of approximately 110 ± 5 nm.

Characterization: The thickness of the active layers was measured using a Stylus profilometer made by Bruker, USA. J–V characteristics were measured using a Keithley 2400 source meter under AM1.5G light (100 mW cm^{-2}) using a Class AAA Newport solar simulator.

Contact angle analysis: Contact angle analysis was conducted using a contact angle goniometer, (Model: L2004A, made by Ossila) equipped with software version 4.0. The instrument has an angle measurement range of 5° to 180° and a resolution of ±0.1°. The surface energies (γ) were calculated from the contact angles by the Wu model[61,62] using the following equations,

$$\gamma_{water}(1 + cos\theta_{water}) = \frac{4\gamma_{water}^{d}\gamma^{d}}{\gamma_{water}^{d} + \gamma^{d}} + \frac{4\gamma_{water}^{p}\gamma^{p}}{\gamma_{water}^{p} + \gamma^{p}} \quad (1)$$

$$\gamma_{DMSO}(1 + cos\theta_{DMSO}) = \frac{4\gamma_{DMSO}^{d}\gamma^{d}}{\gamma_{DMSO}^{d}+\gamma^{d}} + \frac{4\gamma_{DMSO}^{p}\gamma^{p}}{\gamma_{DMSO}^{p}+\gamma^{p}}, \quad (2)$$

$$\gamma \quad = \gamma^{d} + \gamma^{p}. \quad (3)$$

Here, γ_{water} and γ_{DMSO} are the surface energies of water and dimethyl sulfoxide (DMSO), respectively, where γ_{water}^{d} (27.29 mN/m) and γ_{DMSO}^{d} (36 mN/m) are the dispersive component, respectively, and γ_{water}^{p} (44 mN/m) and γ_{DMSO}^{p} (8 mN/m) are the polar component of water and DMSO respectively, θ is the contact angle, γ^{d} and γ^{p} are the dispersive and polar components of the interfacial surface energy. Here, γ_{water} and γ_{DMSO} are equal to 71.29 and 44, respectively.[63,64]

Dynamic mechanical analysis (DMA): The DMA test was conducted using a TA Instruments (DMA-850). The elastomer samples were blade-coated on a clean glass substrate and then transferred to the DMA clips as free free-standing film. All tests were conducted at 0.2% strain and a frequency of 1 Hz, with a preload of 0.03 N and a temperature ramp of 3 °C/min.

Molecular weight measurement: Size Exclusion Chromatography (SEC) measurement was used to determine the molecular weight of the elastomer. SEC was performed on a Waters 2695 separations module liquid chromatograph equipped with two Agilent Resipore columns (PL1113-6300) maintained at 35°C and a Waters 2412 refractive index detector at room temperature. Tetrahydrofuran (THF) was used as the mobile phase at a flow rate of 1.0 mL/min. Molar mass and dispersity data are reported relative to 580−200 000 g/mol poly(styrene) standards.

RSoXS measurement: The resonant soft x-ray scattering (RSoXS) measurements were primarily conducted at beamline 11.0.1.2 at the Advanced Light Source (ALS), Lawrence Berkeley National Laboratory (LBNL). Additionally, two samples were measured at the National Synchrotron Light Source II (NSLS-II) developed and operated by the National Institute of Standards and Technology (NIST). For sample preparation, PSS films were first cast onto Si substrates, followed by the deposition of organic films. The samples were immersed in deionized water, dissolving the PSS layer and allowing the organic films to float. These floated films were carefully transferred onto 2 mm × 2 mm SiNx membrane windows (Norcada NX5200C) and mounted onto an aluminum rack. Two-dimensional scattering patterns were collected using an in-vacuum charge-coupled device (CCD) camera.

Fracture energy measurement: The fracture energy was measured using a four-point bending experiment. The process began with a 50 mm × 50 mm ITO-glass substrate and casting the ZnO layer via spin-coating process as exercised during device fabrication. Next, the active layers were spin-coated onto the ZnO, maintaining a thickness of approximately 110 nm, similar to those used in the devices. A 10 nm thick MoO_3 layer and a 100 nm thick Al layer were thermally evaporated over the active layer at a pressure of $\sim 10^{-7}$ mbar. Following this, an epoxy encapsulation layer was blade-coated over the metal layer. The epoxy (EPO-TEK 353 ND) was prepared by mixing part A and part B at a 10:1 ratio. Another glass substrate was then placed on top of the entire stack. To prepare the specimen, channels 0.18 mm thick with 5 mm spacing were cut into the stack using a dicing saw (Disco Co., DAD 321). A perpendicular channel, 4/5 of the sample thickness, was then cut at the center of the stack (25 mm from the edge). The stack was cleaved to create 5 mm × 50 mm specimens. A pre-crack notch was introduced at the middle channel of the sample, positioned approximately 4/5ths of the way from the ITO-coated glass substrate. The specimen was loaded into a delaminator test system (DTS Co.) with outer pins spaced 40 mm apart and inner pins spaced 15 mm apart.

The fracture energy was calculated as the critical value of the strain energy release rate using the following formula:

$$G_c = \frac{P_c^2 L^2}{16bhE'} \quad (4)$$

Here, P_c is the critical load obtained from the load-displacement curves, L is the distance between the inner and outer pins, b and h are the specimen's width and half-height, and E′ is the plane strain elastic modulus of the glass substrate (assumed to be 70 GPa with a Poisson's ratio of 0.24).

Viscosity measurement: The intrinsic viscosity of various SEPS and SEBS elastomers was determined using an A&D Vibro Viscometer (SV-1A) at room temperature (25°C). Samples were dissolved in chloroform at a concentration of 1 mg/mL and allowed to equilibrate before measurement. The instrument operates based on a tuning fork vibration principle, providing viscosity values in centipoise (cP or mPa·s).

Grazing-incidence wide-angle X-ray scattering (GIWAXS): The GIWAXS measurements were performed using a Xeuss 3.0 X-ray scattering instrument with a Copper K_α source (λ=1.5413 Å). The sample-to-detector distance is 75 mm, and the incident angle was set to 0.2° to maximize scattering intensity. The scattering data was collected using an Eiger 1M detector with a total of 1h exposure with two images (each 30 min) stitched together. 2D GIWAXS patterns were processed using INSIGHT, a Python-based software[65] and the data reduction was analyzed using a modified Nika package in IgorPro 8.38.[66] Scattering peaks were fitted using Lmfit package in Python with a linear background in the composite of π-π peak and halo-ring of the elastomer.[67] The integrated peak area ratio between two peaks was used to quantify the percentage of semiconducting materials and elastomer, respectively. Peaks were fitted with a pseudo-Voigt function. The lamellar stacking distance (d_{100}) and π–π stacking distance (d_{010}) were calculated from the peak positions from 1D line profiles GIWAXS profiles using Bragg's law:

$$d = \frac{2\pi}{q} \quad (5)$$

where q is the scattering vector corresponding to the peak maximum.

The crystal coherence length (CCL) was estimated from the full width at half maximum (FWHM) of the (100) peak using the Scherrer equation:

$$CCL = \frac{2\pi K}{FWHM} \quad (6)$$

where K is a shape factor (0.9).

Supporting information

Details on materials, device fabrication, contact angle measurements, viscosity analysis, fracture testing, RSoXS, and GIWAXS analysis are provided. Additional figures and tables include molecular weight data, surface energy and miscibility parameters, RSoXS/GIWAXS profiles, and full photovoltaic and mechanical performance metrics.

Corresponding Author

*Brendan O'Connor: btoconno@ncsu.edu

Acknowledgement

This work was supported by Office of Naval Research (ONR) N00014-24-1-2101. S.M. and H.A. acknowledge Goodnight Innovation Dist. Professor Endowment for X-ray data acquisition. The Xeuss 3.0 at NCSU has been purchased with ONR grant N000142412143. X-ray measurements were performed at the Advanced Light Source (ALS), which is supported by the Director of the Office of Science, Office of Basic Energy Sciences, U.S. Department of Energy under Contract No. DE-AC02-05CH11231. This research used beamline 7-ID (SST-1) of the National Synchrotron Light Source II, a U.S. Department of Energy (DOE) Office of Science User Facility operated for the DOE Office of Science by Brookhaven National Laboratory under Contract No. DE-SC0012704.

References

(1) Delgado Andrés, R.; Berestok, T.; Shchyrba, K.; Fischer, A.; Würfel, U. A New Figure of Merit for Solar Charging Systems: Case Study for Monolithically Integrated Photosupercapacitors Composed of a Large-Area Organic Solar Cell and a Carbon Double-Layer Capacitor. *Solar RRL* 2022, *6* (10).

(2) Zeng, R.; Zhu, L.; Zhang, M.; Zhong, W.; Zhou, G.; Zhuang, J.; Hao, T.; Zhou, Z.; Zhou, L.; Hartmann, N.; Xue, X.; Jing, H.; Han, F.; Bai, Y.; Wu, H.; Tang, Z.; Zou, Y.; Zhu, H.; Chen, C.-C.; Zhang, Y.; Liu, F. All-Polymer Organic Solar Cells with Nano-to-Micron

Hierarchical Morphology and Large Light Receiving Angle. *Nat Commun* 2023, *14* (1), 4148.

(3) Hashemi, S. A.; Ramakrishna, S.; Aberle, A. G. Recent Progress in Flexible–Wearable Solar Cells for Self-Powered Electronic Devices. *Energy Environ Sci* 2020, *13* (3), 685–743.

(4) Lee, J.; Seo, S.; Lee, S.; Kim, G.; Han, S.; Phan, T. N.; Lee, S.; Li, S.; Kim, T.; Lee, J.; Kim, B. J. Intrinsically Stretchable, Highly Efficient Organic Solar Cells Enabled by Polymer Donors Featuring Hydrogen-Bonding Spacers. *Advanced Materials* 2022, *34* (50).

(5) Ravishankar, E.; Booth, R. E.; Hollingsworth, J. A.; Ade, H.; Sederoff, H.; DeCarolis, J. F.; O'Connor, B. T. Organic Solar Powered Greenhouse Performance Optimization and Global Economic Opportunity. *Energy Environ Sci* 2022.

(6) Shafe, A. Al; O'Connor, B. T. Mechanics of Flexible and Stretchable Organic Electronics. In *Mechanics of Flexible and Stretchable Electronics*; Wiley, 2024; pp 139–169.

(7) Xiao, C.; Li, W. Potential Applications of Organic Solar Cells. In *Organic Solar Cells*; Wiley, 2022; pp 645–676.

(8) Kim, H. J.; Lee, M. Y.; Kim, J.-S.; Kim, J.-H.; Yu, H.; Yun, H.; Liao, K.; Kim, T.-S.; Oh, J. H.; Kim, B. J. Solution-Assembled Blends of Regioregularity-Controlled Polythiophenes for Coexistence of Mechanical Resilience and Electronic Performance. *ACS Appl Mater Interfaces* 2017, *9* (16), 14120–14128.

(9) Booth, R. E.; Schrickx, H. M.; Hanby, G.; Liu, Y.; Qin, Y.; Ade, H.; Zhu, Y.; O'Connor, B. T. Silver Nanowire Composite Electrode Enabling Highly Flexible, Robust Organic Photovoltaics. *Solar RRL* 2022, *6* (9).

(10) Balar, N.; Rech, J. J.; Henry, R.; Ye, L.; Ade, H.; You, W.; O'Connor, B. T. The Importance of Entanglements in Optimizing the Mechanical and Electrical Performance of All-Polymer Solar Cells. *Chemistry of Materials* 2019, *31* (14), 5124–5132.

(11) Balar, N.; Connor, B. T. O. Correlating Crack Onset Strain and Cohesive Fracture Energy in Polymer Semiconductor Films. 2017, 8611–8618.

(12) Kitchen, B.; Awartani, O.; Kline, R. J.; McAfee, T.; Ade, H.; O'Connor, B. T. Tuning Open-Circuit Voltage in Organic Solar Cells with Molecular Orientation. *ACS Appl Mater Interfaces* 2015, *7* (24), 13208–13216.

(13) Zhou, K.; Xian, K.; Ye, L. Morphology Control in High-efficiency All-polymer Solar Cells. *InfoMat* 2022, *4* (4).

(14) Park, J. S.; Kim, G.; Lee, S.; Lee, J.; Li, S.; Lee, J.; Kim, B. J. Material Design and Device Fabrication Strategies for Stretchable Organic Solar Cells. *Advanced Materials* 2022, *34* (31).

(15) Ding, G.; Chen, T.; Wang, M.; Xia, X.; He, C.; Zheng, X.; Li, Y.; Zhou, D.; Lu, X.; Zuo, L.; Xu, Z.; Chen, H. Solid Additive-Assisted Layer-by-Layer Processing for 19% Efficiency Binary Organic Solar Cells. *Nanomicro Lett* 2023, *15* (1), 92.

(16) Lv, J.; Tang, H.; Huang, J.; Yan, C.; Liu, K.; Yang, Q.; Hu, D.; Singh, R.; Lee, J.; Lu, S.; Li, G.; Kan, Z. Additive-Induced Miscibility Regulation and Hierarchical Morphology Enable 17.5% Binary Organic Solar Cells. *Energy Environ Sci* 2021, *14* (5), 3044–3052.

(17) Seo, S.; Lee, J.; Kim, D. J.; Lee, D.; Phan, T. N.; Park, J.; Tan, Z.; Cho, S.; Kim, T.; Kim, B. J. Poly(Dimethylsiloxane)- *Block* -PM6 Polymer Donors for High-Performance and Mechanically Robust Polymer Solar Cells. *Advanced Materials* 2023, *35* (24).

(18) Li, S.; Gao, M.; Zhou, K.; Li, X.; Xian, K.; Zhao, W.; Chen, Y.; He, C.; Ye, L. Achieving Record-high Stretchability and Mechanical Stability in Organic Photovoltaic Blends with a Dilute-absorber Strategy. *Advanced Materials* 2023.

(19) Wang, Z.; Zhang, D.; Xu, M.; Liu, J.; He, J.; Yang, L.; Li, Z.; Gao, Y.; Shao, M. Intrinsically Stretchable Organic Solar Cells with Simultaneously Improved Mechanical Robustness and Morphological Stability Enabled by a Universal Crosslinking Strategy. *Small* 2022, *18* (26).

(20) Solak, E. K.; Irmak, E. Advances in Organic Photovoltaic Cells: A Comprehensive Review of Materials, Technologies, and Performance. *RSC Adv* 2023, *13* (18), 12244–12269.

(21) Yi, J.; Zhang, G.; Yu, H.; Yan, H. Advantages, Challenges and Molecular Design of Different Material Types Used in Organic Solar Cells. *Nat Rev Mater* 2023, *9* (1), 46–62.

(22) Liu, C.; Xiao, C.; Xie, C.; Zhu, Q.; Chen, Q.; Ma, W.; Li, W. Insulating Polymers as Additives to Bulk-Heterojunction Organic Solar Cells: The Effect of Miscibility. *ChemPhysChem* 2022, *23* (2).

(23) Guan, C.; Xiao, C.; Liu, X.; Hu, Z.; Wang, R.; Wang, C.; Xie, C.; Cai, Z.; Li, W. Non-Covalent Interactions between Polyvinyl Chloride and Conjugated Polymers Enable Excellent Mechanical Properties and High Stability in Organic Solar Cells. *Angewandte Chemie International Edition* 2023, *62* (44).

(24) Lee, J.; Nguyen, T. H.; Oh, E. S.; Lee, S.; Choi, J.; Kwon, H. S.; Wang, C.; Lee, S.; Lee, J.; Kim, T.; Kim, B. J. Establishing Co-Continuous Network of Conjugated Polymers and Elastomers for High-Performance Polymer Solar Cells with Extreme Stretchability. *Adv Energy Mater* 2024, *14* (26).

(25) Zhou, K.; Xian, K.; Qi, Q.; Gao, M.; Peng, Z.; Liu, J.; Liu, Y.; Li, S.; Zhang, Y.; Geng, Y.; Ye, L. Unraveling the Correlations between Mechanical Properties, Miscibility, and Film Microstructure in All-Polymer Photovoltaic Cells. *Adv Funct Mater* 2022, *32* (30), 2201781.

(26) Xu, Z.; Han, Y.; Bai, Y.; Chen, X.; Guo, J.; Zhang, L.; Gong, C.; Luo, Q.; Zhang, T.; Ma, C.-Q. Thermoplastic Elastomer Enhanced Interface Adhesion and Bending Durability for Flexible Organic Solar Cells. *npj Flexible Electronics* 2022, *6* (1), 56.

(27) Zhang, J.; Chen, Q.; Li, M.; Zhang, G.; Zhang, Z.; Deng, X.; Xue, J.; Zhao, C.; Xiao, C.; Ma, W.; Li, W. Carboxylating Elastomer via Thiol-Ene Click Reaction to Improve Miscibility with Conjugated Polymers for Mechanically Robust Organic Solar Cells with Efficiency of 19%. *Advanced Materials* 2024, *36* (19).

(28) Lee, H.-G.; Lee, J.-W.; Oh, E. S.; Lee, M. J.; Kim, T.-S.; Lee, C.; Kim, B. J. The Effect of Rigid-Block Length in Elastomer-Containing Photoactive Block Copolymers on the Photovoltaic and Mechanical Properties of Polymer Solar Cells. *J Mater Chem A Mater* 2024, *12* (30), 19039–19051.

(29) Shafe, A. Al; Schrickx, H. M.; Ding, K.; Ade, H.; O'Connor, B. T. Rubber-Toughened Organic Solar Cells: Miscibility–Morphology–Performance Relations. *ACS Energy Lett* 2023, *8* (9), 3720–3726.

(30) Zheng, X.; Wu, X.; Wu, Q.; Han, Y.; Ding, G.; Wang, Y.; Kong, Y.; Chen, T.; Wang, M.; Zhang, Y.; Xue, J.; Fu, W.; Luo, Q.; Ma, C.; Ma, W.; Zuo, L.; Shi, M.; Chen, H. Thorough Optimization for Intrinsically Stretchable Organic Photovoltaics. *Advanced Materials* 2024, *36* (11).

(31) McDowell, C.; Abdelsamie, M.; Zhao, K.; Smilgies, D.; Bazan, G. C.; Amassian, A. Synergistic Impact of Solvent and Polymer Additives on the Film Formation of Small Molecule Blend Films for Bulk Heterojunction Solar Cells. *Adv Energy Mater* 2015, *5* (18).

(32) Li, J.; Colantoni, E.; Temiño, I.; Branchini, P.; Tortora, L.; Mas-Torrent, M. Dopant Diffusion Inhibition in Organic Field-Effect Transistors Using Organic Semiconductor/High-Molecular-Weight Polymer Blends. *Chemistry of Materials* 2023, *35* (4), 1527–1536.

(33) Makita, T.; Sasaki, M.; Annaka, T.; Sasaki, M.; Matsui, H.; Mitsui, C.; Kumagai, S.; Watanabe, S.; Hayakawa, T.; Okamoto, T.; Takeya, J. Spontaneously Formed High-Performance Charge-Transport Layers of Organic Single-Crystal Semiconductors on Precisely Synthesized Insulating Polymers. *Appl Phys Lett* 2017, *110* (16).

(34) Nikzad, S.; Wu, H.-C.; Kim, J.; Mahoney, C. M.; Matthews, J. R.; Niu, W.; Li, Y.; Wang, H.; Chen, W.-C.; Toney, M. F.; He, M.; Bao, Z. Inducing Molecular Aggregation of Polymer Semiconductors in a Secondary Insulating Polymer Matrix to Enhance Charge Transport. *Chemistry of Materials* 2020, *32* (2), 897–905.

(35) Peña-Alcántara, A.; Nikzad, S.; Michalek, L.; Prine, N.; Wang, Y.; Gong, H.; Ponte, E.; Schneider, S.; Wu, Y.; Root, S. E.; He, M.; Tok, J. B. -H.; Gu, X.; Bao, Z. Effect of Molecular Weight on the Morphology of a Polymer Semiconductor–Thermoplastic Elastomer Blend. *Adv Electron Mater* 2023, *9* (9).

(36) Guan, H.; Liao, Q.; Huang, T.; Geng, S.; Cao, Z.; Zhang, Z.; Wang, D.; Zhang, J. Solid Additive Enables Organic Solar Cells with Efficiency up to 18.6%. *ACS Appl Mater Interfaces* 2023, *15* (21), 25774–25782.

(37) Yu, R.; Shi, R.; He, Z.; Zhang, T.; Li, S.; Lv, Q.; Sha, S.; Yang, C.; Hou, J.; Tan, Z. Thermodynamic Phase Transition of Three-Dimensional Solid Additives Guiding

Molecular Assembly for Efficient Organic Solar Cells. *Angewandte Chemie International Edition* 2023, *62* (40).

(38) Balar, N.; Rech, J. J.; Siddika, S.; Song, R.; Schrickx, H. M.; Sheikh, N.; Ye, L.; Megret Bonilla, A.; Awartani, O.; Ade, H.; You, W.; O'Connor, B. T. Resolving the Molecular Origin of Mechanical Relaxations in Donor–Acceptor Polymer Semiconductors. *Adv Funct Mater* 2022, *32* (4), 2105597.

(39) Yang, Q.; Chen, X.; He, Z.; Lan, F.; Liu, H. The Glass Transition Temperature Measurements of Polyethylene: Determined by Using Molecular Dynamic Method. *RSC Adv* 2016, *6* (15), 12053–12060.

(40) Maurer, J. J. Relation between Glass Transition Temperature and Composition of Ethylene Propylene Copolymers. *Rubber Chemistry and Technology* 1965, *38* (4), 979–990.

(41) Aldrich, S. Thermal Transitions of Homopolymers: Glass Transition & Melting Point. *Verfügbar unter: https://www. sigmaaldrich. com/technicaldocuments/articles/materials-science/polymer-science/thermal-transitions-ofhomopolymers. html.(Zugegriffen: 1* 2019.

(42) Rieger, J. The Glass Transition Temperature of Polystyrene. *Journal of Thermal Analysis* 1996, *46* (3–4), 965–972.

(43) Fox, T. G.; Flory, P. J. Second-Order Transition Temperatures and Related Properties of Polystyrene. I. Influence of Molecular Weight. *J Appl Phys* 1950, *21* (6), 581–591.

(44) Chen, H.; Jeong, S. Y.; Tian, J.; Zhang, Y.; Naphade, D. R.; Alsufyani, M.; Zhang, W.; Griggs, S.; Hu, H.; Barlow, S.; Woo, H. Y.; Marder, S. R.; Anthopoulos, T. D.; McCulloch, I.; Lin, Y. A 19% Efficient and Stable Organic Photovoltaic Device Enabled by a Guest Nonfullerene Acceptor with Fibril-like Morphology. *Energy Environ Sci* 2023, *16* (3), 1062–1070.

(45) Guo, Y.; Liu, J.; Lu, Y.; Dong, D.; Wang, W.; Zhang, L. A Combined Molecular Dynamics Simulation and Experimental Method to Study the Compatibility between Elastomers and Resins. *RSC Adv* 2018, *8* (26), 14401–14413.

(46) Xu, L.; Kim, S.; Venkataswamy, K. Novel Thermoplastic Elastomers with Universal Bonding Characteristics. *Rubber world* 2008, *239* (1).

(47) Huang, J.; Xu, Y.; Qi, S.; Zhou, J.; Shi, W.; Zhao, T.; Liu, M. Ultrahigh Energy-Dissipation Elastomers by Precisely Tailoring the Relaxation of Confined Polymer Fluids. *Nat Commun* 2021, *12* (1), 3610.

(48) Lu, Y.; Wang, Y.; Jiang, Z.; Men, Y. Molecular Weight Dependency of Surface Free Energy of Native and Stabilized Crystallites in Isotactic Polypropylene. *ACS Macro Lett* 2014, *3* (11), 1101–1105.

(49) Fritzsching, K. J.; Mao, K.; Schmidt-Rohr, K. Avoidance of Density Anomalies as a Structural Principle for Semicrystalline Polymers: The Importance of Chain Ends and Chain Tilt. *Macromolecules* 2017, *50* (4), 1521–1540. (50) Ye, L.; Stuard, S. J.; Ade, H. Soft X-

Ray Scattering Characterization of Polymer Semiconductors. In *Conjugated Polymers*; CRC press, 2019; pp 427–458.

(51) Ade, H.; Hitchcock, A. P. NEXAFS Microscopy and Resonant Scattering: Composition and Orientation Probed in Real and Reciprocal Space. *Polymer (Guildf)* 2008, *49* (3), 643–675.

(52) Jiao, X.; Ye, L.; Ade, H. Quantitative Morphology–Performance Correlations in Organic Solar Cells: Insights from Soft X-Ray Scattering. *Adv Energy Mater* 2017, *7* (18).

(53) Zheng, Z.; Awartani, O. M.; Gautam, B.; Liu, D.; Qin, Y.; Li, W.; Bataller, A.; Gundogdu, K.; Ade, H.; Hou, J. Efficient Charge Transfer and Fine-Tuned Energy Level Alignment in a THF-Processed Fullerene-Free Organic Solar Cell with 11.3% Efficiency. *Advanced Materials* 2017, *29* (5).

(54) Dupont, S. R.; Voroshazi, E.; Heremans, P.; Dauskardt, R. H. Adhesion Properties of Inverted Polymer Solarcells: Processing and Film Structure Parameters. *Org Electron* 2013, *14* (5), 1262–1270.

(55) Lee, J. W.; Jeong, D.; Kim, D. J.; Phan, T. N. L.; Park, J. S.; Kim, T. S.; Kim, B. J. Flexible-Spacer Incorporated Polymer Donors Enable Superior Blend Miscibility for High-Performance and Mechanically-Robust Polymer Solar Cells. *Energy Environ Sci* 2021, *14* (7), 4067–4076.

(56) Fu, Z.; Wang, T.; Zhang, W.-Q.; Qiao, J.-W.; Cui, F.-Z.; Yin, H.; Du, X.-Y.; Wei, Q.; Hao, X.-T. Structural-Evolution Dynamics and Structural-Defect Suppression in High-Efficiency All-Polymer Solar Cells via Dilution Effect. *PRX Energy* 2023, *2* (4), 043012.

(57) Qi, Q.; Ke, H.; Ye, L. Ternary Organic Solar Cells Featuring Polythiophene. *Energy Materials* 2022, *2* (5), 35.

(58) Holden, G.; Kricheldorf, H. R.; Quirk, R. P. *Thermoplastic Elastomers*; Thermoplastic Elastomers; Hanser, 2004.

(59) *Unveiling the Distinctions in Properties and Applications of SEBS and SEPS Polymers*. https://www.grand-petrochemical.com/blog/Unveiling-the-Distinctions-in-Properties-and-Applications-of-SEBS-and-SEPS-Polymers/.

(60) Zhang, F.; Mohammadi, E.; Qu, G.; Dai, X.; Diao, Y. Orientation-Dependent Host–Dopant Interactions for Manipulating Charge Transport in Conjugated Polymers. *Advanced Materials* 2020, *32* (39).

(61) Neu, J.; Oh, J.; Mukherjee, S.; Kashani, S.; Chen, Z.; Mardiev, S.; Ade, H.; You, W. Tuning the Solubility Parameters of Conjugated Polymers via Side-Chain Engineering for All-Polymer Solar Cells. *Chemistry of Materials* 2025, *37* (10), 3788–3798.

(62) Wu, S. Calculation of Interfacial Tension in Polymer Systems. *Journal of Polymer Science Part C: Polymer Symposia* 1971, *34* (1), 19–30.

(63) Wu, S. Polar and Nonpolar Interactions in Adhesion. *J Adhes* 1973, *5* (1), 39–55.

(64) Zdziennicka, A.; Krawczyk, J.; Szymczyk, K.; Jańczuk, B. Components and Parameters of Liquids and Some Polymers Surface Tension at Different Temperature. *Colloids Surf A Physicochem Eng Asp* 2017, *529*, 864–875.

(65) Cantin, S.; Bouteau, M.; Benhabib, F.; Perrot, F. Surface Free Energy Evaluation of Well-Ordered Langmuir–Blodgett Surfaces. *Colloids Surf A Physicochem Eng Asp* 2006, *276* (1–3), 107–115.

(66) Reus, M. A.; Reb, L. K.; Kosbahn, D. P.; Roth, S. V.; Müller-Buschbaum, P. INSIGHT: In Situ Heuristic Tool for the Efficient Reduction of Grazing-Incidence X-Ray Scattering Data. *J Appl Crystallogr* 2024, *57* (2), 509–528.

(67) Ilavsky, J. Nika: Software for Two-Dimensional Data Reduction. *J Appl Crystallogr* 2012, *45* (2), 324–328.

(68) *https://lmfit.github.io/lmfit-py/*.

ToC Figure